



# Photocatalytic degradation of ethylene using titanium dioxide nanotube arrays with Ag and reduced graphene oxide irradiated by $\gamma$ -ray radiolysis

Quan Zhang, Shengying Ye\*, Xuemei Chen, Xianliang Song, Liqin Li, Xun Huang

College of Food Science, South China Agricultural University, Wushan, Guangzhou, Guangdong 510640, PR China



## ARTICLE INFO

### Article history:

Received 16 June 2016

Received in revised form

30 September 2016

Accepted 12 October 2016

Available online 13 October 2016

### Keywords:

Photocatalytic

Titanium dioxide nanotube arrays

Reduced graphene oxide

Silver nanoparticles

Ethylene

Gamma rays

## ABSTRACT

Titanium dioxide nanotube arrays (TNTAs) made by anodic oxidation method and irradiated under  $^{60}\text{Co-}\gamma$  radiation combining with silver nanoparticles (AgNPs) and reduced graphene oxide (rGO) irradiated by  $^{60}\text{Co-}\gamma$  rays as well were investigated for photocatalytic degradation of ethylene in cold storage environment. Rate constant  $K$  of degradation was selected to describe the decomposition efficiency of ethylene with the new photocatalytic composite material (AgNPs/rGO-TNTAs). Microstructure of the materials as prepared were characterized using analytic techniques: Atomic Force Microscope (AFM), Raman Spectroscopy, Fourier Transform Infrared Spectroscopy (FTIR), Field Emission Scanning Electron Microscope (FESEM), Transmission Electron Microscope (TEM), X-ray Diffraction (XRD) and X-ray Photoelectron Spectroscopy (XPS). We also compared the performance of five photocatalysts (Thermal annealing TNTAs,  $^{60}\text{Co-}\gamma$ -TNTAs, AgNPs- $^{60}\text{Co-}\gamma$ -TNTAs, AgNPs/rGO- $^{60}\text{Co-}\gamma$ -TNTAs) concerning ethylene decomposition. Results showed that AgNPs/rGO- $^{60}\text{Co-}\gamma$ -TNTAs exhibited enhancement of photocatalytic degradation of ethylene compared with rGO- $^{60}\text{Co-}\gamma$ -TNTAs and AgNPs- $^{60}\text{Co-}\gamma$ -TNTAs in photocatalytic process. Photocatalytic activity and structural evolution of photocatalysts irradiated by gamma rays and impact of the photocatalysts properties responsible for enhancing photocatalytic activity were discussed.

© 2016 Elsevier B.V. All rights reserved.

## 1. Introduction

Fruits and vegetables are highly sensitive to ethylene ( $\text{C}_2\text{H}_4$ ) which plays an important role in storage environment of horticultural products after harvest. As a plant hormone, high concentration of ethylene can accelerate softening and corruption of fruits and vegetables, leading to a bad storage quality in preserved processing and shorten shelf life during the sale period [1]. Due to the existence of ethylene in closed environment of products and inappropriate storage methods we adopted, great economic losses have been made every year. It is estimated that losses as high as 10–80% have been caused out of the harmful impact of ethylene on horticultural products [2]. Thus removing sources of  $\text{C}_2\text{H}_4$  from the postharvest environment of horticultural commodities are one of the main challenges that we faced to be solved urgently [3].

Titanium dioxide nanotube arrays (TNTAs) have large specific surface area, stable chemical properties, no pollution in reaction and it can be reused with highly ordered and vertical growth

characteristics. Besides, ordered array structure and lower agglomeration degrees between nanotubes also determine high quantum effects of TNTAs to make the photo-generated electrons ( $e^-$ ) and hole ( $h^+$ ) pairs own stronger reduction ability under ultraviolet light. It is reported that TNTAs have been applied widely in micro extraction techniques, enzyme immobilization, catalytic activity, energy storage materials and aluminum ion batteries [4–8]. However, only if the photo-generated  $e^-$  and  $h^+$  pairs are not recombined each other, will TNTAs show a strong reduction activity under the UV light. During the practical circumstance, the  $e^-$  and  $h^+$  pairs are easy to recombine and restrain the application of TNTAs in photocatalytic degradation severely [9]. The modification to TNTAs would be an effective way to solve the recombination of  $e^-$  and  $h^+$  pairs and lot of interests have aroused the attention of researchers in the aspects. Zhu et al. [10] reported Pt/CdS combined with TNTAs could enhance photocatalytic performance and Zeng et al. [11] reported that ZnO by atomic layer deposition would improve photocatalytic degradation property of TNTAs. There are few reports on the improvement of the photocatalytic decomposition of ethylene with TNTAs modified by both reduced graphene oxide (rGO) and silver nanoparticles (AgNPs).

\* Corresponding author.

E-mail addresses: [yesy@scau.edu.cn](mailto:yesy@scau.edu.cn), [13424453381@163.com](mailto:13424453381@163.com) (S. Ye).

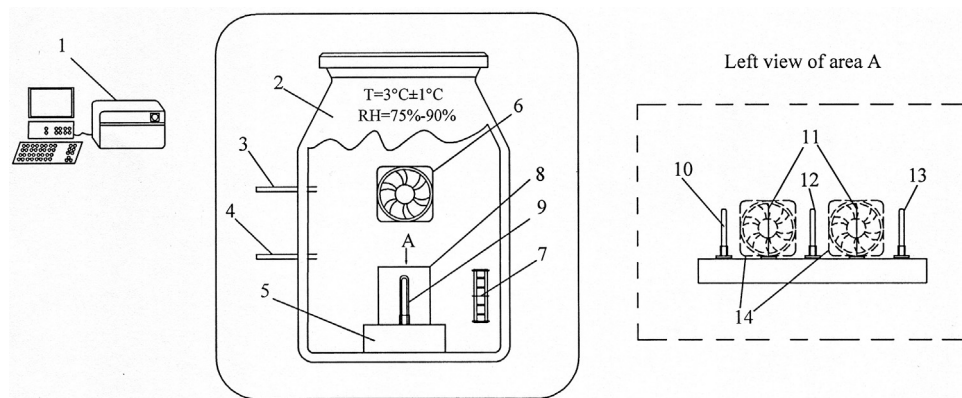


**Fig. 1.** Schematic representation of the experimental setup: (1) gas chromatograph; (2) cylindrical vessel; (3) ethylene outlet; (4) ethylene inlet; (5) base stand; (6,7,14) axial-flow fan; (8,11) TNTAs-samples; (9,10,12,13) UV lamp.

Graphene is currently the world's thinnest but the most rigid two-dimensional material [12]. Compared with other carbon materials, graphene present lower resistivity and faster electron transfer ratio, it is suitable for making transparent electrode and touch screen as a good conductor with high specific surface area. In addition, it is widely used in some fields like new energy materials, energy conversion and storage, tissue engineering and biomedical application [13–16]. Graphene is easy to combine with nanostructure materials to compose some compounds. If graphene can be modified to the surface of TNTAs to make it as an excellent carrier for the photo-generated  $e^-$  and  $h^+$  pairs, it will help to achieve a separation of photo-generated carrier ( $h^+/e^-$ ). Furthermore, photocatalytic degradation performance of the semiconductor materials will be greatly improved through combining rGO with silver nanoparticles (AgNPs) on the surface of TNTAs to form the three elements network. Strategies for preparing graphene at present mainly include micro mechanical stripping method, liquid phase stripping method, epitaxial growth method, chemical reduction method and so on. High qualities of graphene are got by micro mechanical stripping method, but the yield is very low and products need to be screened in a lot of different thickness of graphite flakes which spend too much manpower and material resources [17]. Lower concentration of graphene solution is prepared by using liquid phase stripping method and epitaxial growth method requires complex hydrothermal progress [18,19]. Although there are many chemical routes available for production of reduced graphene oxide (rGO), it is still desirable to design a rapid and large-scale synthesis for this material. Gamma radiation, also known as gamma rays ( $\gamma$ -rays), is an electromagnetic radiation of high frequency and therefore high energy. Compared with the traditional reduction methods, gamma ray irradiation reduction technology has the advantages of no toxicity, no pollution, no need to add the reducing agent, little byproduct, high yield and easy control. We have demonstrated enhancement of the photocatalytic activity of  $TiO_2$  on activated carbon fiber for ethylene removal by Ag nanoparticles synthesized by  $\gamma$ -ray radiolysis [20]. Radiation-induced reduction is considered to be a facile and environmental friendly approach to prepare rGO [21]. The most important thing is that  $\gamma$ -ray radiation has been observed to play a key role in inducing disruption and dislodgement of electrons [22]. TNTAs fabricated by potentiostatic anodization of pure Ti in fluoride-based baths are easily obtained with large surface area in comparison to other methods of synthesis [23,24]. But thermal treatment method involving the use of a muffle furnace at 400–600 °C temperatures and times is needed to convert them into the conductive anatase phase. The nanotubular structure used with the anatase phase crystal structure due to its higher conductivity can promote a rapid separation of charge carri-

ers [25]. However, there is no information exists in the literature for the  $\gamma$ -ray annealing method associated to TNTAs crystal structure changes. The photocatalytic degradation of ethylene in cold storage environment to either gamma ray annealing TNTAs (labeled  $^*TNTAs$  in the present study)-supported rGO prepared by reduction using  $\gamma$ -radiolysis (labeled rGO- $^*TNTAs$ ) or gamma ray annealing TNTAs-supported both AgNPs and rGO prepared by using  $\gamma$ -radiolysis (labeled AgNPs/rGO- $^*TNTAs$ ) have rarely been reported.

In this paper, we prepare rGO and AgNPs with  $\gamma$ -ray radiation technology firstly. Then rGO and AgNPs are doped into the surface of  $^*TNTAs$  to synthesize AgNPs/rGO- $^*TNTAs$ . We also compare the performance of the thermal annealing TNTAs (labeled MF-TNTAs in the present study),  $^*TNTAs$ , AgNPs- $^*TNTAs$ , rGO- $^*TNTAs$  and AgNPs/rGO- $^*TNTAs$  concerning ethylene decomposition, as well as analyze the photocatalytic activity and structural evolution of  $^*TNTAs$ -based materials. The aim of this study is to demonstrate the effectiveness of the  $\gamma$ -irradiation technique in preparing photocatalysts and to make the photocatalytic process more attractive for an air cleaner available in cold storage environments for controlling ethylene.

## 2. Materials and methods

### 2.1. Material and $\gamma$ -ray source

Titanium sheet (TA1, 99.5%) was purchased from Baoji metal materials and equipment manufacturing Co., Ltd. Graphene oxide (GO) powder was purchased from Nanjing Xianfeng nano material technology Ltd. Isopropyl alcohol was used to scavenge the excess radicals and Ag nanoparticles were prepared from silver nitrate ( $AgNO_3$ ). In the  $\gamma$ -irradiation process, polyvinyl pyrrolidone (PVP) K30 (MW = 50000) was used as the stabilizer. Distilled water was used throughout our experiments.

The  $^{60}Co$   $\gamma$ -ray source (Nordion International Co. Ltd., Ontario, Canada) was located at the Guangdong Center of Irradiation Technology. The source strength was approximately  $4 \times 10^6$  Ci and was applied at a dose rate of  $\sim 1$  kGy/h at room temperature.

### 2.2. Preparation of the photocatalytic materials and characterization

The titanium sheet was cut to a size of 95 mm  $\times$  55 mm and polished with waterproof sandpaper (1000#, 2500# and 5000#) sequentially. 500 mL electro polishing liquid was formulated according to the volume ratio of hypochloric acid: ethanol = 1:9 and cooled to 10 °C in cold water bath subsequently. After that, titanium sheet was fixed on the anode and graphite sheet was fixed

on the cathode, both positive and negative surface of the titanium sheet were electrolyzed for 30 s in the electro polishing liquid as we prepared under certain voltage and temperature (10 V, 10 °C), then it was washed with deionized water and dried at 105 °C. With the anodic oxidation method, TNTAs were prepared as follows: pre-processed titanium sheet and graphite sheet were dipped into 65 mm depth of the electrolyte (800 g with 0.5 wt% NH<sub>4</sub>F, 2 wt% H<sub>2</sub>O and ethanediol), then controlled the reaction conditions (voltage 40 V, polar distance 30 mm, temperature 20 °C) for 5 h to get the 55 mm × 65 mm dimension of TNTAs which were irradiated with a total dose of 0, 10, 20 and 30 kGy at room temperature eventually. The products were correspondingly denoted as <sup>\*</sup>TNTAs-0, <sup>\*</sup>TNTAs-10, <sup>\*</sup>TNTAs-20 and <sup>\*</sup>TNTAs-30 in the study. The MF-TNTAs were prepared by using a muffle furnace at 500 °C, 4 h for annealing.

The GO dispersion solution was prepared by adding graphene oxide powder (100 mg) and 1 wt% isopropyl alcohol into deionized water (50 mL) and stripped in 570 W ultrasonic power for 120 min. Treated dispersion solution were irradiated in sealed quartz container under various  $\gamma$ -ray irradiation to get the rGO solution. After this, the rGO solution was drop into the surface of <sup>\*</sup>TNTAs as we described above to form the rGO-<sup>\*</sup>TNTAs. 0.5 wt% silver nitrate was added into 1000 mL purified water to make up silver nitrate solution and right amount of the solution were added PVP and isopropyl alcohol, after that the treated solution were deaerated for 60 min. Colloidal Ag nanoparticles were prepared finally under the  $\gamma$ -ray irradiation and combined with the <sup>\*</sup>TNTAs in a titration manner to make up AgNPs-<sup>\*</sup>TNTAs. The composite AgNPs/rGO-<sup>\*</sup>TNTAs were got by following steps: first, graphite oxide powder (200 mg) and silver nitrate solution (0.5 wt%) were mixed into deionized water with PVP (1 wt%) and isopropanol (1 wt%) added. Then the mixed solution as prepared were stripped under 570 W for 2 h to get homogeneous silver nitrate and reduced graphene oxide dispersion. The dispersion was irradiated by  $\gamma$ -ray irradiation in a quartz container and dropped onto the surface of <sup>\*</sup>TNTAs finally to make up AgNPs/rGO-<sup>\*</sup>TNTAs.

Lamellar structure and degree of graphitization of the reduced graphene oxide was measured by atomic force microscope (AFM, BioScope Catalyst, Veeco) and Raman spectrometer (inVia, Renishaw, England). The surface morphology of AgNPs-<sup>\*</sup>TNTAs, rGO-<sup>\*</sup>TNTAs, AgNPs/rGO-<sup>\*</sup>TNTAs and the distribution of Ag nanoparticle on rGO were observed using field emission scanning electron microscope (FESEM, MeiLin, Zeiss). The samples were cut into a size of 5 × 5 mm and placed on copper table when it was ready for detection. XRD data of MF-TNTAs, <sup>\*</sup>TNTAs-samples, AgNPs-<sup>\*</sup>TNTAs nanocomposite were recorded based on the X-ray diffraction (D/Max-III A, Rigaku Industrial Corporation, Japan). Before testing, the samples were handled by vacuum drying and milled to fine powder. The surface characterization of nanocomposite was determined by using XPS (ESCALAB 250), using an Al K $\alpha$  X-ray source ( $h\nu = 1486.6$  eV) for the excitation of electrons. The analyzer pass energy was 20 eV for high-resolution spectra. The binding energies were referenced to the C 1s peak (284.5 eV) used as internal standard to account for the charging effects. The areas of the peaks were computed by fitting the experimental spectra to Gaussian/Lorentzian curves after removal of the background (Shirley function), and analysis of the selected spectra was deconvolved using XPSPEAK4.1 software. The size distributions of the AgNPs prepared were obtained using a Tecnai12 model Transmission Electron Microscopy (FEI Co, Holland). A drop of the silver colloidal solution was placed on a carbon-coated copper grid, followed by evaporation under vacuum for 25 min.

### 2.3. Experimental structure of the reactor system

In our work, the photocatalytic reactor system designed to decompose ethylene in simulated cold storage environment was

shown schematically in Fig. 1. The photocatalytic device system mainly consisted of a test reactor, DC fans, <sup>\*</sup>TNTAs-samples or MF-TNTAs and UV lamps. The test reactor was a 50 L cylindrical vessel with a removable cap and an ethylene inlet and outlet on the left. The number of the UV light was three and it was emitted from a 12 W ozone-free cold-cathode UV lamp set at a wavelength of 254 nm and projected onto the surface of <sup>\*</sup>TNTAs-samples or MF-TNTAs. Three axial-flow fans were installed in the reactor system to guarantee the adequate contact of ethylene gas mixture with the composite photocatalytic materials. The flow rate in this study was ~0.28 mm<sup>3</sup>/min. The photocatalytic degradation equipment (UV lamps, <sup>\*</sup>TNTAs-samples or MF-TNTAs) were settled on a base stand for fixing and all elements in experimental reactor system were introduced by opening the cap of the cylindrical vessel. The temperature and relative humidity of the reactor were controlled at 3 ± 1 °C and 75–90% through a thermometer and hygrometer in the middle of the facility. Ethylene was quantitatively analyzed using a model GC-7980 II gas chromatograph (Techcomp Ltd., China) equipped with a flame-ionization detector and Teflon syringes (3 mL, gas tight) were used to sample the ethylene.

### 2.4. Procedures and evaluation of photocatalytic degradation of ethylene

Prior to a test, the whole reactor was placed in damp air and the cap on the cylindrical vessel was open to allow the air in the room enter the vessel for circulating with the UV lamps turned off. After this, the cap was closed and high pure ethylene (3 mL) were injected into the reactor through the inlet. While 240 min was chosen to act as an adsorption equilibrium time for countering the adverse effects of ethylene absorption by the reactor system components, which would otherwise disturb the accuracy of ethylene degradation. After 240 min, the concentration of ethylene was detected using GC for three times and each interval was 15 min. The average concentration of the three experiments was determined to set the initial concentration of ethylene. Then turned on the three UV lamps and fans to start the photocatalytic degradation. The concentration of ethylene was monitored by extracting samples for analysis at 30 min interval for eight times continuously.

It was reported that the kinetic equation of photocatalytic degradation accorded with the model of Langmuir-Hinshelwood (L-H) and it presented a pseudo-first-order reaction when ethylene was at millimolar concentration [26]. The kinetics may be expressed as  $\ln(C_t/C_0) = Kt$ , where  $K$  was the apparent rate constant that we adopted to assess the photocatalytic degradation of ethylene by <sup>\*</sup>TNTAs-samples or MF-TNTAs and  $C_0, C_t$  were the concentration of ethylene initially and at time  $t$ , respectively.

Data reduction and analysis for the whole study used Origin-Pro7.5 software (Origin Lab Corp.).

## 3. Results and discussion

### 3.1. Characterization

AFM was used to test the structure, thickness and the size of the reduced graphene oxide that prepared to modify <sup>\*</sup>TNTAs. Fig. 2 exhibited the cross-sectional view of as-prepared rGO. The slice size was measured in the range of 0–450 nm and the thickness of the thin layer was about 3.5 nm, and the middle part of rGO was significantly higher than that in the adjacent area. This was most likely because the folding part, that is, the folding of the sheet led to a significant increase in the thickness of rGO.

Raman spectra of the GO and as-prepared rGO were presented in Fig. 3. rGO displayed two typical bands located at 1357 cm<sup>-1</sup> for D band and 1603 cm<sup>-1</sup> for G band. The D band is ascribed to

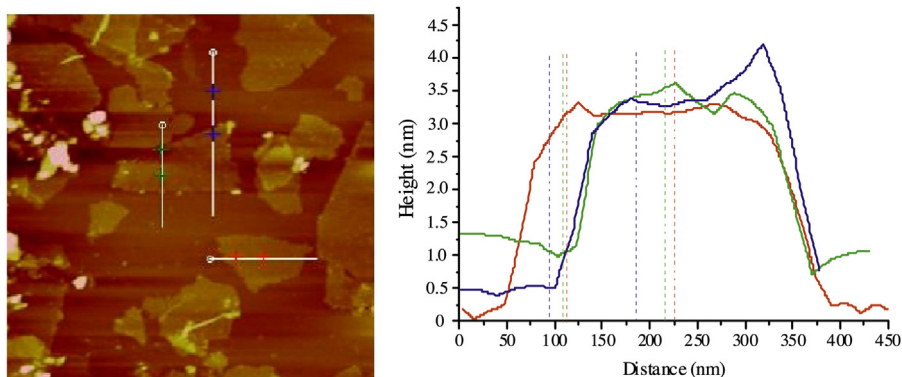


**Fig. 2.** Atomic force microscopic diagram of the as-prepared rGO (For interpretation of the references to colour in this figure legend, the reader is referred to the web version of this article).

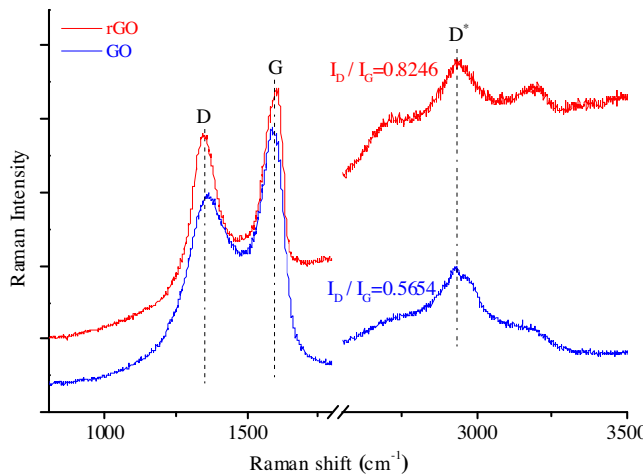


**Fig. 3.** Raman spectrum of graphene oxide and as-prepared reduced graphene oxide.

edge or in-plane  $sp^3$  defects and disordered carbon, whereas the G band arises from in-plane vibration of ordered  $sp^2$ -bonded carbon atoms in two dimensional hexagonal lattice. In general, the  $I_D/I_G$  intensity ratio is a measure of the relative concentration of local defects/disorders and average size of the  $sp^2$  domains in graphite materials. Particular note was the  $I_D/I_G$  ratio increased to 0.8246 for rGO prepared by  $\gamma$ -ray reduction as compared with 0.7248 of GO, this may be explained by that the large number of  $sp^3$  hybrid carbon atoms would form the defects and disorders to  $sp^2$  region after reduction [27,28].

FESEM micrograph of AgNPs-<sup>\*</sup>TNTAs-20 showed the surface of the titanium substrate was presented with ordered and vertically aligned nanotubes in Fig. 4(a). As prepared rGO-<sup>\*</sup>TNTAs-20 (Fig. 4(b)), we could find the lamellar structure of rGO and some fold state of marginal sections, which could be attributed to the existence of oxygen-containing groups and loose structure of prepared rGO. Lamellar and folded layer structures were superimposed on each other due to the incomplete stripping. As for AgNPs/rGO-<sup>\*</sup>TNTAs-20, the nanotube diameter measured was about 60–80 nm and the wall thickness was closed to 5–10 nm from Fig. 4(c), the huge specific surface area of nanotubes could increase the transfer of photo electrons and hole pairs efficiently [29]. Moreover, a small amount of loaded materials of AgNPs and rGO distributed in the outer of nanotubes was also observed which indicated that the loaded material did not enter the interior of the nanotubes. The fine dots on the surface of rGO were predicted to be Ag particles (Fig. 4(d) red arrow).

**Fig. 5** showed XRD pattern of <sup>\*</sup>TNTAs-0, <sup>\*</sup>TNTAs-10, <sup>\*</sup>TNTAs-20 <sup>\*</sup>TNTAs-30, MF-TNTAs, and AgNPs-<sup>\*</sup>TNTAs-20. The peak locations for the samples are cited from the Joint Committee on Powder Diffraction Standards (JCPDSs) database. All the samples had been confirmed to be a  $TiO_2$  with anatase phase dominating except for <sup>\*</sup>TNTAs-0 sample. <sup>\*</sup>TNTAs-0 sample only presented the anatase phase  $TiO_2$  peaks at  $2\theta$  angles of 25.11 and 37.66°, which can be assigned to the (101) and (112) crystal planes of anatase phase. It is interesting to note that methods of either thermal treatment or  $\gamma$ -ray annealing can convert crystal structures of <sup>\*</sup>TNTAs-0 into the anatase phase further. The pattern of AgNPs-<sup>\*</sup>TNTAs-20 showed, in addition to the anatase phase  $TiO_2$  peak, the presence of diffraction peaks at  $2\theta$  angles of 38.09°, 44.20°, 64.43° and 77.47°, which can be assigned to the (111), (200), (220) and (311) crystal planes of face-centered cubic (fcc) structure of Ag crystallite, respectively, according to the standard XRD patterns (JCPDS, No. 4-0783).

Surface defects and chemical changes of <sup>\*</sup>TNTAs-samples induced by  $\gamma$ -ray-irradiation were determined by XPS analysis. Deconvolution of the high resolution scan XPS spectra of (a) <sup>\*</sup>TNTAs-0, (b) <sup>\*</sup>TNTAs-10, (c) <sup>\*</sup>TNTAs-20, (d) <sup>\*</sup>TNTAs-30 for Ti 2p and O 1s were illustrated in Fig. 6(1) and (2). The XPS spectrum for Ti 2p and O 1s at high-resolution scan were showed in Fig. S2–S5 for Supporting information. Fig. 6(1) showed the Ti 2p photoelectron peak at  $E_b$  = 458.75, 458.81, 458.75 and 458.84 for  $Ti^{4+}$  2p3/2 and  $E_b$  = 464.51, 464.60, 464.46 and 464.59 for  $Ti^{4+}$  2p1/2 which were both attributed to  $Ti^{4+}$ . Peaks at different  $E_b$  for  $Ti^{3+}$  2p3/2 and  $Ti^{3+}$  2p1/2 were also listed in this figure. Inset of each diagram at the upper left for Fig. 6(1) displayed partial enlarged details of  $Ti^{3+}$  2p3/2. It can be observed that the weaker peak of  $Ti^{3+}$  2p3/2 in <sup>\*</sup>TNTAs-0 which meant the smaller contribution of  $Ti^{3+}$  for photocatalytic activity without  $\gamma$ -ray radiation. Fig. 6(2) showed the deconvolution of high-resolution scan O 1s spectra of (a) <sup>\*</sup>TNTAs-0, (b) <sup>\*</sup>TNTAs-10, (c) <sup>\*</sup>TNTAs-20, (d) <sup>\*</sup>TNTAs-30. The O 1s spectra can be resolved into three peaks at  $530 \pm 0.5$ ,  $531 \pm 0.5$  and  $532.5 \pm 0.5$  eV for  $O^{2-}$ ,  $\bullet OH$  and  $H_2O$  or C–O, respectively [30]. In the case of  $\gamma$ -irradiated <sup>\*</sup>TNTAs-20, a peak shift of  $\sim 0.26$  and  $\sim 0.02$  eV for hydroxyl group peak and  $O^{2-}$  peak in O 1s was seen relative to <sup>\*</sup>TNTAs-0. Comparison of TNTAs irradiated from 0 to 30 kGy based on the Ti 2p and O 1s, we could find that <sup>\*</sup>TNTAs changed in the Ti 2p3/2 and Ti 2p1/2 spectra as well as  $O^{2-}$  and  $\bullet OH$  in O 1s spectra. In the XPS spectra of element scan, for AgNPs/rGO-<sup>\*</sup>TNTAs-20 (Fig. 7(a)), two peaks of Ag 3d located at 368.45 (Ag 3d3/2) and 374.53 (Ag 3d5/2) eV were observed, which were in good agreement with the previous literature [31], and silver ions reduced into metallic silver by  $\gamma$ -ray irradiation were successfully loaded on the rGO sheets. As shown in Fig. 7(b), the C 1s spectrum of AgNPs/rGO-<sup>\*</sup>TNTAs-20 suggested the abundance of various oxygen-containing functional groups on the rGO surface. (The XPS

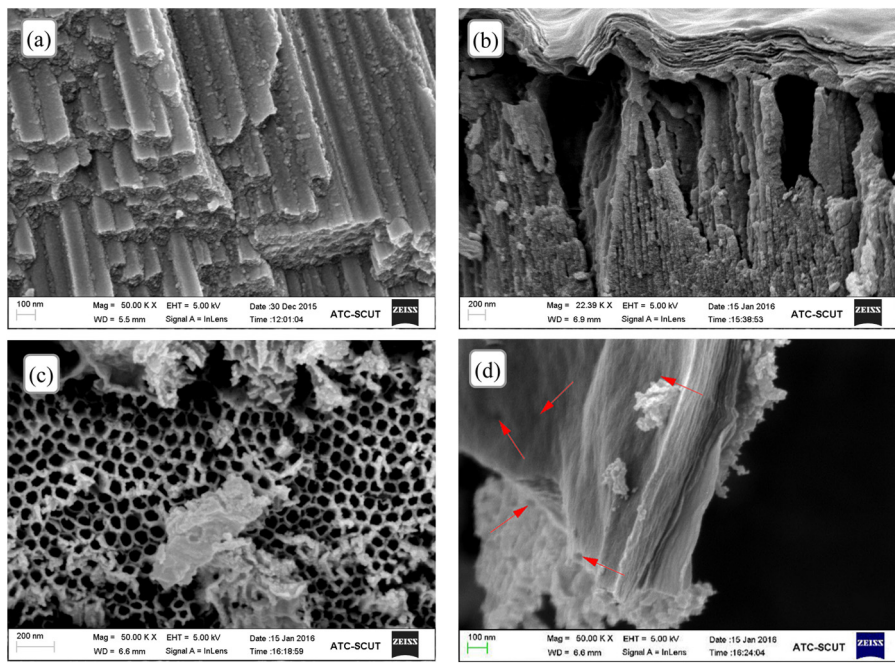


**Fig. 4.** FESEM micrograph of AgNPs-\*TNTAs-20 (a), rGO-\*TNTAs-20 (b), AgNPs/rGO-\*TNTAs-20 (c) and Ag particles dispersed on the rGO (d). (For interpretation of the references to colour in the text, the reader is referred to the web version of this article.)

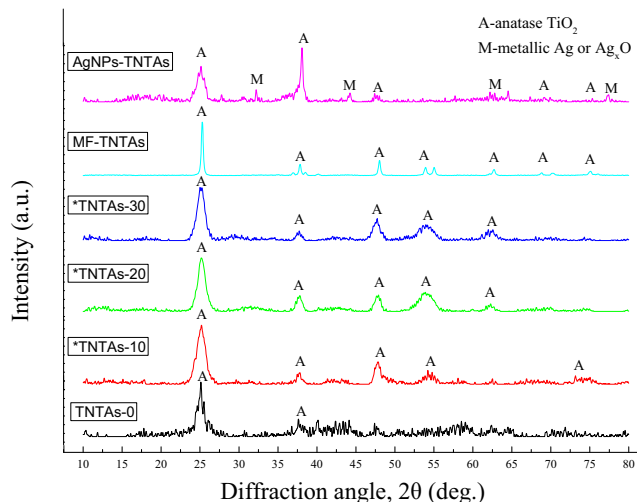


**Fig. 5.** XRD pattern of \*TNTAs-0, \*TNTAs-10, \*TNTAs-20, \*TNTAs-30, MF-TNTAs, and AgNPs-\*TNTAs-20.

survey scan spectrum of AgNPs/rGO-\*TNTAs-20, deconvolution of the high resolution scan XPS spectra of Ti 2p and O 1s were shown in Fig. S1 and Fig. S7 for Supporting information).

### 3.2. Effects of gamma radiation on photocatalytic activity and structural evolution of photocatalysts

To make clear the process of photocatalysts for ethylene degradation, we studied the behavior of gamma rays on the photocatalytic activity and structural evolution of rGO-\*TNTAs-20, AgNPs-\*TNTAs-20 and AgNPs/rGO-\*TNTAs-20 with the rate constant  $K$  as reference.

#### 3.2.1. Effect of gamma irradiation on rGO-\*TNTAs-20

Linear relationship between  $\ln (C_t / C_0)$  and reaction time with various gamma irradiation dose on photocatalyst with per square

meter of \*TNTAs containing 3.83 mg rGO were showed in Fig. 8(a). With the extension of time, the value of  $\ln (C_t / C_0)$  decreased significantly and linear fitting correlation coefficient ( $R^2$ ) of each line was greater than 0.98, which indicated that the reaction was consistent with the first order kinetic model. It is noted that the  $K$  value increases with the increasing irradiation dose to 20 kGy, and thereafter decreases (Fig. 8(b)).

FTIR diagram of GO treated with different irradiation dose by gamma rays was demonstrated in Fig. 9. There were no big differences occurred when GO was irradiated under 10 kGy and 20 kGy, except that in  $1410\text{ cm}^{-1}$ ,  $1226\text{ cm}^{-1}$  and  $1052\text{ cm}^{-1}$  which represented the hydroxyl ( $\text{OH}$ ) deformation absorption peak, C—O stretching vibration peak, respectively. Decreased peak in these wavenumber indicated that epoxy group C—O was susceptible to energy destruction after irradiated by gamma rays from 10 kGy to 30 kGy. Wavenumber at  $1726\text{ cm}^{-1}$  and  $1620\text{ cm}^{-1}$  exhibited the stretching vibration absorption peak of carbonyl ( $\text{C=O}$ ) and deformation absorption peak of adsorbent water molecules on the surface of rGO. Smaller changes had been observed at these wavenumbers when GO was treated under 10 kGy and 20 kGy, except that treated with 30 kGy which manifested weak absorption peak. This may be explained by that the energy level of the atoms was destroyed when applied higher energy on it. Changes happened at wavenumber about  $3400\text{ cm}^{-1}$  which presented hydroxyl ( $\text{OH}$ ) vibration absorption peak and applied  $\gamma$ -ray irradiation promoted the reduction of GO to rGO to a certain extent. Allaedini et al. [32] have proved that the peak around  $3363\text{ cm}^{-1}$  corresponds to the stretching vibration of  $\text{OH}$ . The transmittance for GO irradiated under 10, 20 and 30 kGy were 42.2, 39.3 and 68.3%, respectively. This results exhibited that GO irradiated under 20 kGy performed the highest hydrophilicity. Guo et al. [33] had reported that the high hydrophilicity could increase adsorption capacity to the gaseous reactants and prevent water condensation in the surface of  $\text{TiO}_2$  photocatalyst materials cavities. The photocatalytic activity of  $\text{TiO}_2$ -samples studied is further confirmed by the changes in hydroxyl ( $\text{OH}$ ) vibration absorption peak [34]. FTIR diagram of rGO is a good candidate for an explanation of the phenomena observed.

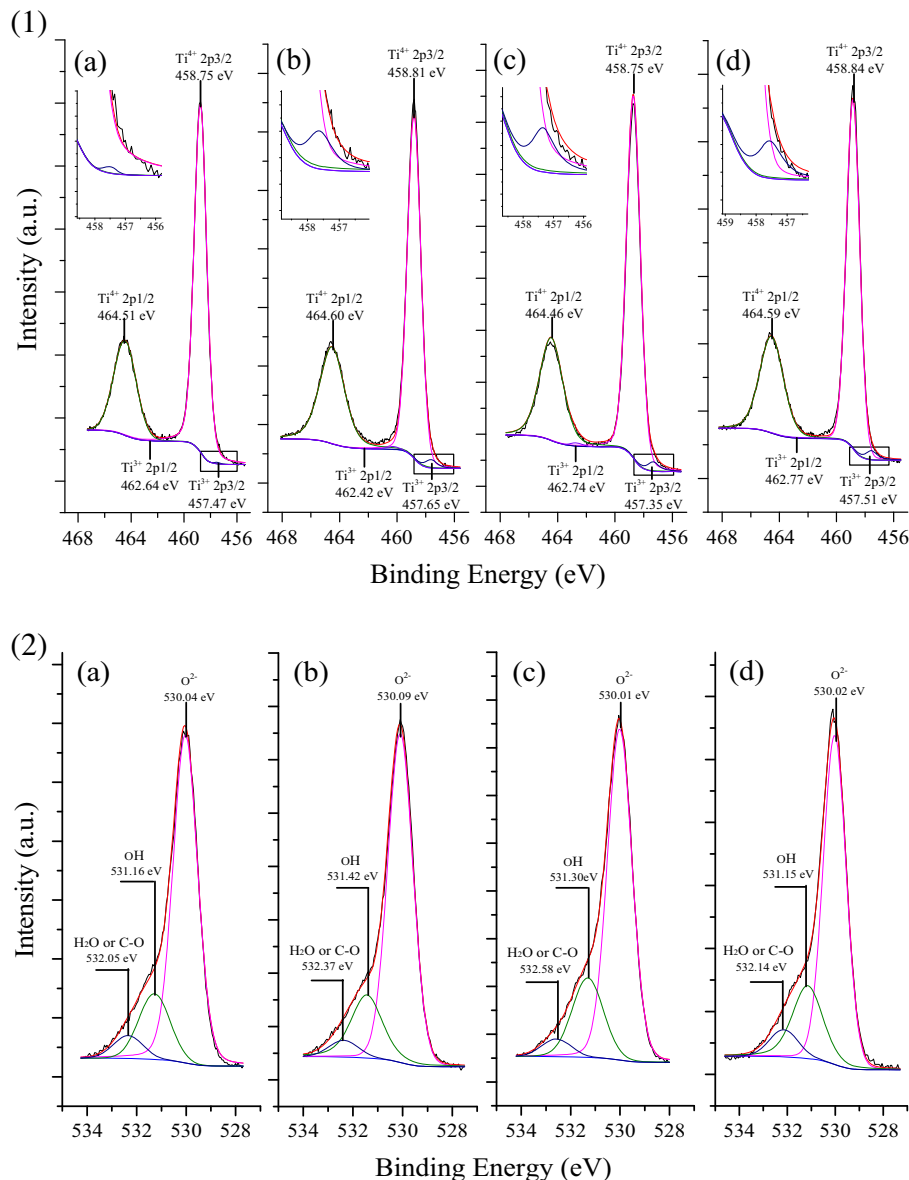


**Fig. 6.** (1) Deconvolution of high-resolution scan Ti 2p spectra of (a) \*TNTAs-0, (b) \*TNTAs-10, (c) \*TNTAs-20, (d) \*TNTAs-30. Partial enlarged detail of  $\text{Ti}^{3+}$  2p3/2 was inserted into the upper left of each diagram. Line in black, red and blue presented as Raw Intensity, Peak Sum and Background respectively. (2) Deconvolution of high-resolution scan O 1s spectra of (a) \*TNTAs-0, (b) \*TNTAs-10, (c) \*TNTAs-20, (d) \*TNTAs-30. Line in black, red and blue presented as Raw Intensity, Peak Sum and Background respectively. (For interpretation of the references to colour in this figure legend, the reader is referred to the web version of this article.)

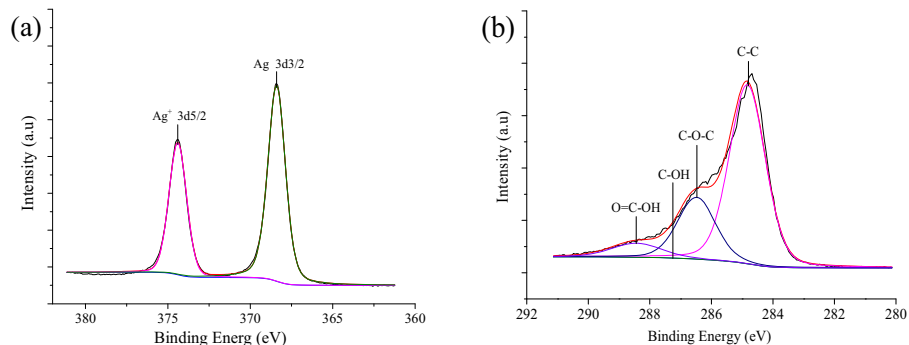


**Fig. 7.** Deconvolution of high-resolution scan XPS spectra of (a) Ag 3d and (b) C 1s in AgNPs/rGO- \*TNTAs-20. Line in black, red and blue presented as Raw Intensity, Peak Sum and Background respectively. (For interpretation of the references to colour in this figure legend, the reader is referred to the web version of this article.).

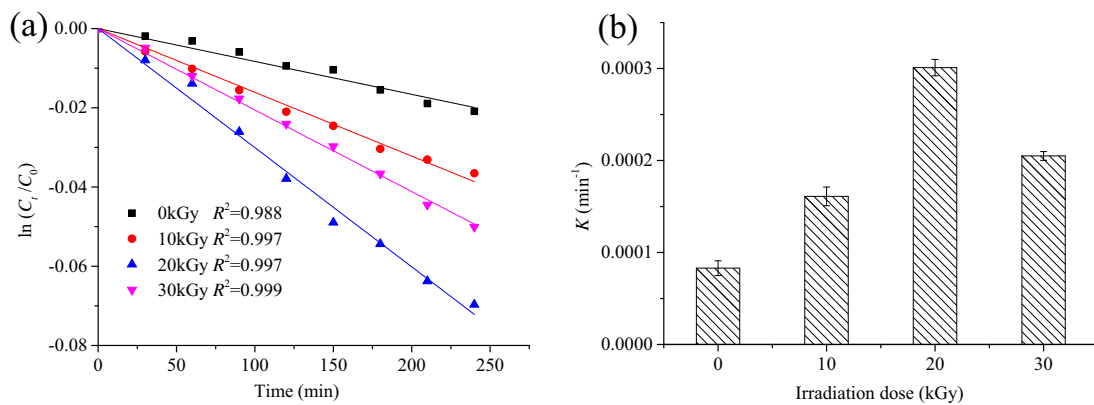


**Fig. 8.** Effect of Gamma irradiation dose and rGO- \*TNTAs-20 on (a) Kinetic curves for ethylene reduction with  $\ln(C_t/C_0)$  against reaction time and (b) Dependence of irradiation dose on the  $K$  value for  $C_2H_4$  degradation.

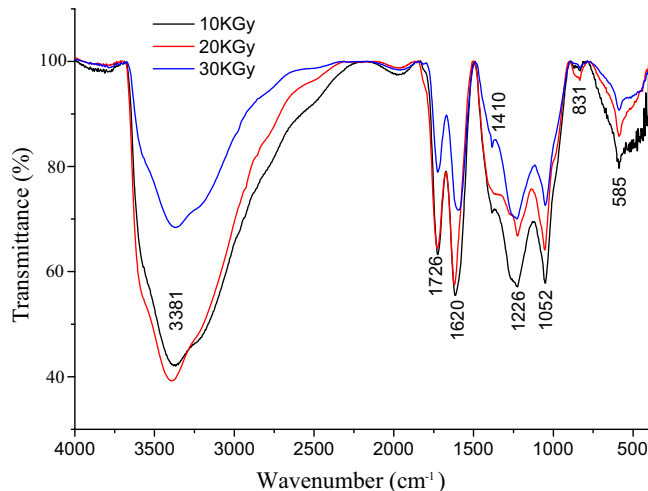


**Fig. 9.** FTIR diagram of GO treated with 10, 20 and 30 kGy irradiation dose.

### 3.2.2. Effect of gamma irradiation on AgNPs- \*TNTAs-20

Fig. 10(a) showed the effect of gamma radiation on the photocatalytic activity of AgNPs- \*TNTAs-20 with per square millimeter of \*TNTAs containing 0.0012 mg AgNPs for ethylene degradation. Equations with different irradiation dose on AgNPs exhibited first-kinetic due to the goodness of fit and the regression coefficients ( $R^2$ ) > 0.99 in all cases. It was interesting to observe that the  $K$  value increased first and then decreased with the increase of gamma irra-

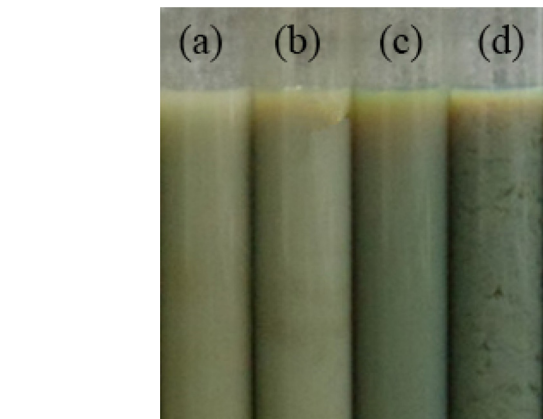


**Fig. 11.** Photographs of colloidal AgNPs obtained under various  $\gamma$ -irradiation doses: (a) 10 kGy, (b) 20 kGy, (c) 30 kGy, (d) 40 kGy.

diation (Fig. 10(b)). Where 20 kGy would be the optimum treatment by gamma rays on photocatalyst for good  $K$  value and the count was about 0.000316 min<sup>-1</sup>.

Photographs of colloidal AgNPs obtained under various  $\gamma$ -irradiation doses from 10 kGy to 40 kGy were recorded in Fig. 11. Agglomeration phenomenon became more and more obvious with the increasing dose of  $\gamma$ -irradiation as the picture showed. The phenomenon of agglomeration began to occur evidently when AgNPs were irradiated at 30 kGy and significant changes were observed at 40 kGy with a large number of flocculent precipitate presented.

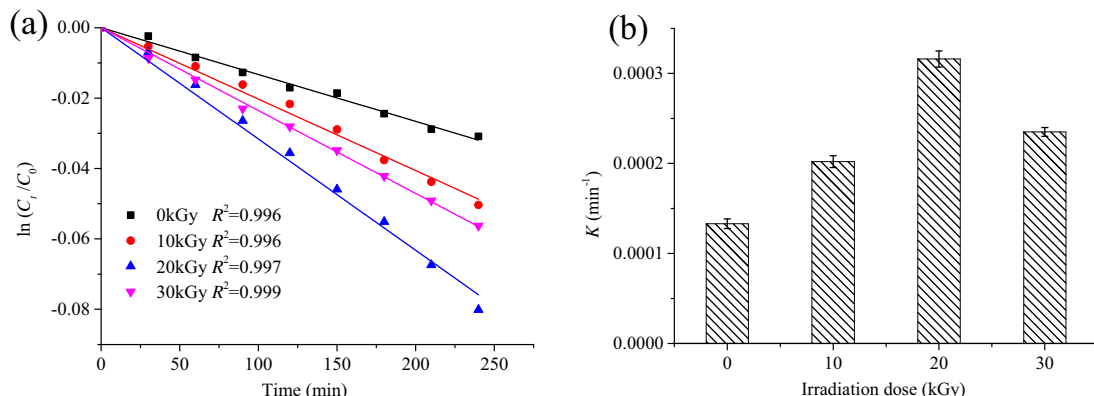


**Fig. 10.** Effect of Gamma irradiation dose and AgNPs- \*TNTAs-20 on (a) Kinetic curves for ethylene reduction with  $\ln(C_t/C_0)$  against reaction time and (b) Dependence of irradiation dose on the  $K$  value for  $C_2H_4$  degradation.

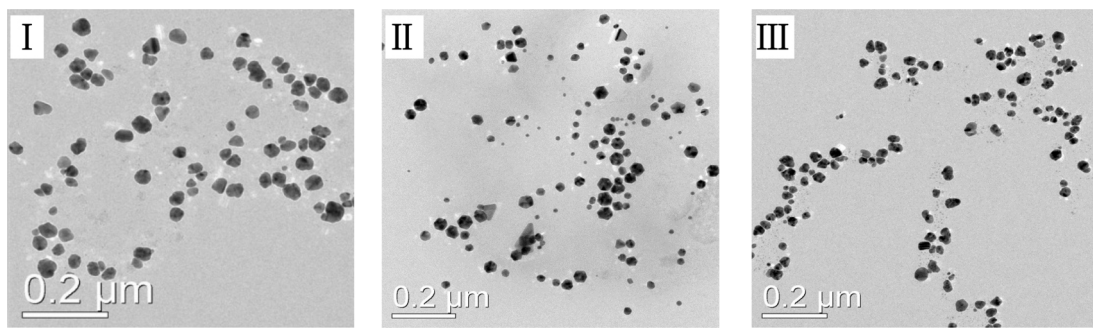


Fig. 12. TEM micrograph for AgNPs prepared by various  $\gamma$ -irradiation doses: I) 10 kGy, II) 20 kGy, III) 30 kGy.

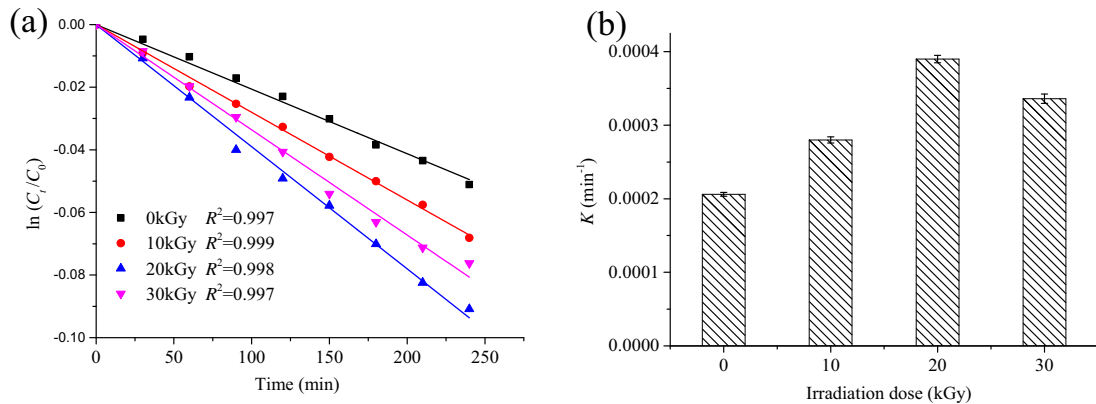


Fig. 13. Effect of Gamma irradiation dose and AgNPs/rGO-‐TNTAs-20 on (a) Kinetic curves for ethylene reduction with  $\ln (C_t /C_0)$  against reaction time and (b) Dependence of irradiation dose on the  $K$  value for  $\text{C}_2\text{H}_4$  degradation.

In order to determine the size of the AgNPs, TEM photographs were used to measure the nanometer size of the Ag particles. The average particle sizes of AgNPs and their corresponding standard deviations at each radiation dose (10, 20 and 30 kGy) with 1 wt% content of PVP in the solutions are  $38.54 \pm 5.35$ ,  $23.62 \pm 4.67$  and  $23.56 \pm 5.04$  nm in Fig. 12. The average particle sizes and their corresponding standard deviations became smaller and narrower with increasing radiation dose from 10 kGy to 20 kGy. In addition, the particle size is probably related to the amount of stabilizing polymer chains. With increasing radiation dose to 30 kGy, the individual macromolecules of PVP are assumed to become crosslinked with one another, giving rise to a three-dimensional network. The crosslinking of polymer molecules results in a significant increase in molecular mass. The more polymer chains there are, the more they inhibit the aggregation and/or growth of the AgNPs. Effect of AgNPs on the photocatalytic properties is dependent on the size of these particles, which determines the ratio of absorption to scattering of the incident light.

### 3.2.3. Effect of gamma irradiation on AgNPs/rGO-‐TNTAs-20

Effect of different gamma irradiation dose for preparing AgNPs/rGO doped on \*TNTAs-20 to decompose ethylene were presented in Fig. 13(a). Irradiation doses were set at 0, 10, 20 and 30 kGy throughout the experiments. First order kinetic model was proved on the basis of the linear fitting correlation coefficient ( $R^2 > 0.997$ ). The good rate constant  $K$  value ( $0.000390 \text{ min}^{-1}$ ) appeared when irradiation dose was 20 kGy to prepare AgNPs and rGO (Fig. 13(b)). According to the contents mentioned above, the structure of AgNPs and rGO may play one of important roles in AgNPs/rGO-‐TNTAs-20 for photocatalytic activities.

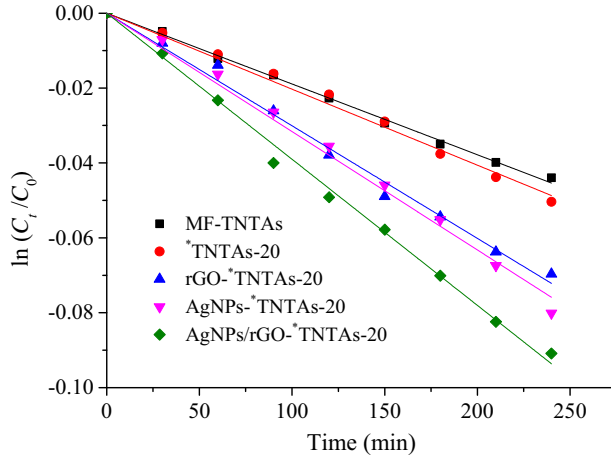
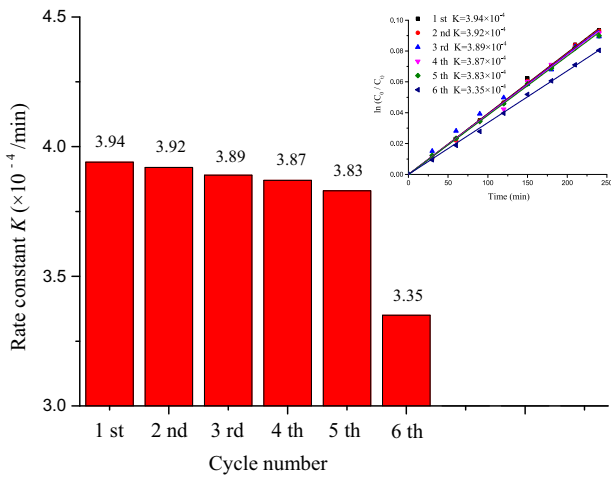
It is supposed that the main reasons for the lower  $K$  value after the radiation dose of 20 kGy are: (i) the corresponding standard deviation of the AgNPs size is larger at the 30 kGy radiation doses may be rationalized in terms of  $\gamma$ -rays inducing chains cissions in the polymer matrix. This liberates the AgNPs once more, allowing crystals to aggregate and/or agglomerate. Radiation at 30 kGy doses may start to destroy the solvation shell of the growing colloid particles and disrupt the charge equilibrium on their surface (ii) significant changes of GO under the radiation dose of 20 kGy mainly leads to the enhanced hydroxyl (\*OH) vibration absorption peak which could be attributed to the highest hydrophilicity for stronger adsorption capacity of ethylene and weaker water condensation of TNTAs cavities.

### 3.3. Rates of photocatalytic materials in ethylene degradation process

Comparison of five photocatalytic materials in ethylene degradation process, namely, MF-TNTAs, \*TNTAs-20, rGO-‐TNTAs-20, AgNPs-‐TNTAs-20 and AgNPs/rGO-‐TNTAs-20 was carried out in experimental reactor system. Kinetic curves for ethylene degradation using five TNTAs-based photocatalytic materials were displayed in Fig. 14. Table 1 summarized degradation kinetic parameters: rate constant, regression equation and the regression coefficients corresponding to four \*TNTAs-based and MF-TNTAs photocatalytic materials, respectively. It can be found that ethylene can be degraded at a certain degree under 5 photocatalytic materials and the  $K$  values of photocatalytic process (PC) with the \*TNTAs-based photocatalysts are higher than that of the MF-TNTAs, indicating that efficient degradation of ethylene is achieved using \*TNTAs-based photocatalysts. The difference in  $K$  value

**Table 1**Rate constants ( $K$ ) value calculated on the basis of the first order reaction kinetics.

Photocatalytic materials	Regression equation	$R^2$	Rate constant, $K^a$ (min $^{-1}$ )
MF-TNTAs	$\ln(C_t/C_0) = -0.000189 \cdot t$	0.999	$1.89 \times 10^{-4}$
*TNTAs-20	$\ln(C_t/C_0) = -0.000203 \cdot t$	0.997	$2.03 \times 10^{-4}$
rGO <sup>b</sup> -TNTAs-20	$\ln(C_t/C_0) = -0.000307 \cdot t$	0.997	$3.07 \times 10^{-4}$
AgNPs-*TNTAs-20	$\ln(C_t/C_0) = -0.000316 \cdot t$	0.997	$3.16 \times 10^{-4}$
AgNPs/rGO-*TNTAs-20	$\ln(C_t/C_0) = -0.000390 \cdot t$	0.998	$3.90 \times 10^{-4}$

<sup>a</sup> Rate constant was identified from the slope of  $\ln(C_t/C_0)$ , slope =  $-K$ .<sup>b</sup> rGO preparation parameters: ultrasonic power of 570 W, ultrasonic time of 120 min.<sup>c</sup> AgNPs/rGO preparation parameters: ultrasonic power of 570 W, ultrasonic time of 120 min.**Fig. 14.** Kinetic curves for ethylene reduction using MF-TNTAs, \*TNTAs-20, rGO-\*TNTAs-20, AgNPs-\*TNTAs-20, AgNPs/rGO-\*TNTAs-20.**Fig. 15.** Repeated experiments for the photocatalytic degradation of ethylene with AgNPs/rGO-\*TNTAs-20.

between rGO-\*TNTAs-20 and AgNPs/rGO-\*TNTAs-20 with \*TNTAs-20 is  $1.04 \times 10^{-4}$  min $^{-1}$  and  $1.87 \times 10^{-4}$  min $^{-1}$ , respectively. The combinations of the AgNPs/rGO-doped on \*TNTAs-20 have a beneficial effect to enhancing the rate of the PC degradation of ethylene.

The repeated experiments for the photocatalytic degradation of ethylene were performed in experimental reactor system for evaluating the photochemical stability of the AgNPs/rGO-\*TNTAs. The  $K$  values of the present photocatalyst were kept little changes at less than 3% when used repeatedly for five times, and decreased from the 6th run (Fig. 15). The fall in the photocatalytic activity of the catalysts, probably as a result of adsorption of  $O_2$  and  $H_2O$  molecules

on the surface of the present composites, means decrease of active sites.

### 3.4. Effects of the properties of photocatalysts on PC performance

The changes of properties of photocatalysts would alter their photocatalytic activity on the surface toward ethylene degradation, affecting the efficiency of PC processes.

Surface defects changes of TNTAs induced by the  $\gamma$ -ray irradiation were determined by XRD analysis. Table 2 summarize the anatase phase mean crystallite dimension and unit cell parameters of \*TNTAs-0, \*TNTAs-10, \*TNTAs-20, \*TNTAs-30 and MF-TNTAs from the data obtained concerning XRD patterns. It is worthy to note that the mean crystallite dimension and unit cell volume decreased to 7.0 nm and  $0.1221 \text{ nm}^3$  for \*TNTAs-20 as compared with 7.29 nm and  $0.1360 \text{ nm}^3$  of \*TNTAs-10. The structural data showed that the  $a$  &  $b$ -axis lattice parameter of the anatase in TNTAs irradiated by  $\gamma$ -ray did not change generally, while the  $c$ -axis lattice parameter of anatase slightly decreased. The reason of this decrease was probably an evolution of chemically and physically bound water. Thus, it is inferred that the unit cell volume greatly shrank along  $c$ -axis. The analysis of anatase phase mean crystallite dimension, unit cell parameters and XRD patterns (Fig. 5) indicated that  $\gamma$ -irradiation not only increased the anatase phase transformation of TNTAs but also decreased the both mean crystallite dimension and unit cell volume of the anatase phase. As a mean crystallite dimension gets smaller, its surface area increases, and the surface atoms have easier mobility, which leads to greater defects, thus further enlarging lattice deformation. More surface area promotes greater efficiency of light and substance absorption on the surface, which increases the decomposition area and degradation activity of the catalyst toward organic gases.

Quantitative analysis of the chemical changes of TNTAs induced by the  $\gamma$ -ray-irradiation was accomplished by XPS. After deconvolution using Gaussian–Lorentzian functions, the Ti 2p core level spectra of  $\gamma$ -irradiated TNTAs showed four peaks due to  $Ti^{3+}$  2p3/2,  $Ti^{4+}$  2p3/2,  $Ti^{3+}$  2p1/2 and  $Ti^{4+}$  2p1/2, respectively (Fig. 6(1)). The relative ratios of the  $Ti^{3+}$  and  $Ti^{4+}$  states in the surface of different samples are shown in Table 3. The ratio of  $Ti^{4+}$  in the Ti ion of \*TNTAs-0 was 99.83%, while the ratio of  $Ti^{3+}$  occupied only about 0.17% and contribution of  $Ti^{3+}$  for the photocatalytic activity in this case was so small. Following  $\gamma$ -ray treated on TNTAs samples from 0 to 30 kGy, the ratios of  $Ti^{3+}$  ( $Ti^{3+}$  2p3/2 and  $Ti^{3+}$  2p1/2) in the Ti ion increased as a function of irradiation dose while the ratios of  $Ti^{4+}$  decreased in general. About 2.48% and 2.72% of  $Ti^{3+}$  2p was observed in the Ti ion of \*TNTAs-20 and AgNPs-\*TNTAs (Deconvolution of the high resolution scan XPS spectra of Ti 2p and O 1s were shown in Fig. S6 for Supporting information), which indicated that the addition of irradiated silver increased the  $Ti^{3+}$  content to a certain extent. More  $Ti^{3+}$  surface state favored the separation of electron–hole pairs and provided important reactive agents for many adsorbates [37]. The enhanced photocatalytic activity of AgNPs-\*TNTAs may be explained by the formation of Schottky barrier between AgNPs and \*TNTAs-20 and the function of  $Ti^{3+}$  described above. For AgNPs-

**Table 2**Anatase phase mean crystallite dimension and unit cell parameters of <sup>\*</sup>TNTAs-0, <sup>\*</sup>TNTAs-10, <sup>\*</sup>TNTAs-20, <sup>\*</sup>TNTAs-30 and MF-TNTAs.

Samples	Mean crystallite dimension <sup>a</sup> (nm)	Unit cell parameters		
		<i>a=b</i> <sup>b</sup> (nm)	<i>c</i> (nm)	Volume <sup>c</sup> (nm <sup>3</sup> )
<sup>*</sup> TNTAs-0	17.53	0.3740	1.1081	0.1550
<sup>*</sup> TNTAs-10	7.29	0.3802	0.9034	0.1360
<sup>*</sup> TNTAs-20	7.0	0.3806	0.8428	0.1221
<sup>*</sup> TNTAs-30	6.7	0.3805	0.8426	0.1220
MF-TNTAs	12.35	0.3786	0.9499	0.1362

<sup>a</sup> Calculated by Scherrer's equation [35]:  $d = \xi \lambda / (\beta \cos \theta)$ , where  $d$  is the crystallite size (nm),  $\xi$  is the constant (shape factor about 0.9),  $\lambda$  is the X-ray wavelength (nm),  $\beta$  is the full width at half maximum (FWHM) of the diffraction line (rad), and  $\theta$  is the diffraction angle (rad).

<sup>b</sup> Calculated by Bragg's formula [36]:  $4 \sin^2 \theta / \lambda^2 = [(h^2 + k^2)/a^2] + (l^2/c^2)$ , where  $h$ ,  $k$  and  $l$  are Miller indices; and  $a$  and  $c$  are lattice parameters. For the tetragonal system, the conditions of the three lattice parameters are  $a=b \neq c$ . The  $\theta$  value in all samples were used based on the  $2\theta$  assigned to the (101) and (200) crystal planes of anatase phase, except that <sup>\*</sup>TNTAs-0 which calculated according to the  $2\theta$  assigned to the (101) and (112) crystal planes of anatase phase.

<sup>c</sup> Calculated from the product among the three lattice parameters.

**Table 3**High-resolution XPS of Ti 2p and O1s peak deconvolution and possible groups on the surface of <sup>\*</sup>TNTAs-samples, AgNPs-<sup>\*</sup>TNTAs-20 and AgNPs/rGO-<sup>\*</sup>TNTAs-20.

Samples	Contribution of Ti 2P components (%)				Contribution of O 1s components (%)		
	Ti <sup>3+</sup> 2P3/2	Ti <sup>4+</sup> 2P3/2	Ti <sup>3+</sup> 2P1/2	Ti <sup>4+</sup> 2P1/2	O <sup>2-</sup>	•OH	H <sub>2</sub> O or C—O
<sup>*</sup> TNTAs-0	0.14	68.68	0.03	31.15	76.09	17.99	5.92
<sup>*</sup> TNTAs-10	1.68	62.33	0.47	35.52	75.03	20.59	4.38
<sup>*</sup> TNTAs-20	1.99	64.89	0.49	32.63	73.65	21.88	4.47
<sup>*</sup> TNTAs-30	2.09	65.32	0.51	32.08	70.14	22.82	7.04
AgNPs- <sup>*</sup> TNTAs-20	2.14	62.54	0.58	34.74	69.85	22.76	7.39
AgNPs/rGO- <sup>*</sup> TNTAs-20	2.21	65.56	0.54	31.60	71.40	24.56	4.04

<sup>\*</sup>TNTAs-20 and AgNPs/rGO-<sup>\*</sup>TNTAs-20, the total amount of Ti<sup>3+</sup> and Ti<sup>4+</sup> changed without remarkable signs, though it was noted to find the increased amount of Ti<sup>3+</sup> 2p3/2 in AgNPs/rGO-<sup>\*</sup>TNTAs-20. Responsible for the enhancement of photocatalytic activity of AgNPs/rGO-<sup>\*</sup>TNTAs-20 could link to the strong conduction electron capability and highest hydrophilicity of prepared rGO. The quantitative variation of these matter in the <sup>\*</sup>TNTAs surface of different samples was obtained from the O 1s spectra and showed in Table 3 as well. The amount of •OH adsorption increased and O<sup>2-</sup> decreased with the dose of  $\gamma$ -irradiation treated on TNTAs from 0 to 30 kGy. Though 22.82% ratio of •OH occupied in <sup>\*</sup>TNTAs-30 compared with the 21.88% ratio in <sup>\*</sup>TNTAs-20, the 7.04% ratio of H<sub>2</sub>O or C—O in <sup>\*</sup>TNTAs-30 which increased by about 36.51% compared with the 4.47% ratio in <sup>\*</sup>TNTAs-20. The higher amount of H<sub>2</sub>O or C—O adsorbed on the surface of <sup>\*</sup>TNTAs, the lower photocatalytic activity would be due to the relative blocked interaction between ethylene and materials. Compared the contribution of O 1s components in AgNPs-<sup>\*</sup>TNTAs-20 and AgNPs/rGO-<sup>\*</sup>TNTAs-20, the amount of O<sup>2-</sup> decreased by 2.17% and •OH increased by about 7.33%. Maximum amount of •OH generated by AgNPs/rGO-<sup>\*</sup>TNTAs-20 among all TNTAs-samples could prove that composite AgNPs/rGO played an important role in improving •OH contents. The produced •OH had been considered to be the major active species responsible for the photocatalytic oxidation reaction and a certain concentration of hydroxyl could attack the adsorbed pollutant molecules to produce oxidized species and/or decomposed organic products [38]. On the whole, chemical changes to the <sup>\*</sup>TNTAs surface induced by ions, electrons and neutral species of  $\gamma$ -irradiation resulted in an enhancement of Ti<sup>3+</sup> and hydroxyl radical for the advance of photocatalytic activity.

Above observations were due to the fact that an enhancement of Ti<sup>3+</sup>, hydroxyl radical and crystallite surface area can act as defects/impurities, decreases recombination and enhances photocatalytic activity.

The application of AgNPs as modifiers of the semiconductor surfaces is one of the methods enabling the entrapment of electrons which results in the longer recombination times of the electron-

hole pairs [39]. The phenomenon responsible for this change is Schottky barrier. In AgNPs-<sup>\*</sup>TNTAs-20, AgNPs cover the small area of the <sup>\*</sup>TNTAs-20 at a Ag content below its optimum level and, after excitation, the electron migrates to the metal, where it becomes trapped (electron-hole recombination is suppressed). The potential in the enhancement of the *K* as demonstrated by the experiment of degradation ethylene using AgNPs-<sup>\*</sup>TNTAs-20 as photocatalyst lies in the presence of the smaller size of AgNPs.

Silver ions were reduced by  $\gamma$ -irradiation and AgNPs distributed on rGO sheets, which was in accordance with the FESEM image of AgNPs/rGO-<sup>\*</sup>TNTAs-20 (Fig. 4(d)). From the high resolution spectra of C 1s (Fig. 7(b)), the oxygen-containing functional groups in the sample can be deconvoluted into C—Cat 284.4 eV, C—OH at 285.0 eV, C—O—C at 286.6 eV, and O=C—OH at 288.43 eV. Abundant oxygen containing functional groups on the rGO make its layer show good electronegativity and provide a large number of sites for the Ag formation by absorbing Ag<sup>+</sup> through electrostatic effect [40]. The presence of graphene with high electrical conductivity can also promote the separation of photo-generated carriers and inhibit the combination of electron-hole pairs [41]. According to Liu et al. [42], the Ag 3d3/2 and Ag 3d5/2 peaks (Fig. 7(a)) can be further divided into two different peaks at 374.6, 374.08 eV and 368.6, 368.05 eV, respectively. The peaks at 374.6 and 368.6 eV resulted from metallic silver. Metallic Ag can efficiently retard the recombination of photo-generated electrons and holes. The interface rGO and TiO<sub>2</sub> particles can narrow the band gap of TiO<sub>2</sub> and was demonstrated by the UV-vis spectrum [43]. In TNTAs-graphene hybrids, graphene can slow the electron-hole pairs, increasing charge transfer rate of electrons and surface-adsorbed amount of chemical molecules through  $\pi$ — $\pi$  interactions [44]. It is a rational corollary that the interface of AgNPs/rGO and TNTAs promoting charge separation and charge transfer. This obvious enhancement effect of AgNPs/rGO-<sup>\*</sup>TNTAs-20 can be explained by the following two ways: (i) that the increase in the crystallite surface area, the Ti<sup>3+</sup> and •OH states reduced the work function of the <sup>\*</sup>TNTAs, and (ii) that the mechanism of variation of photocatalytic activity for AgNPs, rGO/TNTAs and

AgNPs/rGO, as discussed before. It is probable that the ways are happening in parallel.

#### 4. Conclusions

The PC process for  $C_2H_4$  degradation in simulated cold-storage conditions was investigated using titanium dioxide nanotube arrays with Ag and reduced graphene oxide irradiated by  $\gamma$ -ray radiolysis and the following conclusions made:

- (1) Titanium dioxide nanotube arrays was prepared by anodic oxidation and  $\gamma$ -irradiation annealing (\*TNTAs).  $\gamma$ -irradiation at dose of 20 kGy not only increased the anatase phase transformation of TNTAs but also decreased the both mean crystallite dimension of the anatase phase and increased generation of the  $Ti^{3+}$  state and hydroxyl radical.
- (2) AgNPs and rGO were synthesized using a convenient and environment-friendly  $\gamma$ -radiolysis method. The use of AgNPs/rGO-\*TNTAs-20 and AgNPs-\*TNTAs-20 as photocatalyst films led to a higher  $C_2H_4$  decomposition rate constant than rGO-\*TNTAs-20. The order of the  $C_2H_4$  decomposition rate constant ( $K$  value) for the photocatalyst films was AgNPs/rGO-\*TNTAs-20 > AgNPs-\*TNTAs-20 > rGO-\*TNTAs-20.

#### Acknowledgement

Financial support from the National Nature Science Foundation of China (31171449) is gratefully acknowledged by the authors.

#### Appendix A. Supplementary data

Supplementary data associated with this article can be found, in the online version, at <http://dx.doi.org/10.1016/j.apcatb.2016.10.034>.

#### References

- [1] Q. Hu, Y. Fang, Y. Yang, N. Ma, L. Zhao, *Food Res. Int.* 44 (2011) 1589–1596.
- [2] A.A. Kader, *HortScience* 38 (2003) 1004–1008.
- [3] M.L.V. de Chiara, S. Pal, A. Licciulli, M.L. Amodio, G. Colelli, *Biosyst. Eng.* 132 (2015) 61–70.
- [4] M.T. García-Valverde, R. Lucena, S. Cárdenas, M. Valcárcel, *TrAC Trends Anal. Chem.* 62 (2014) 37–45.
- [5] Y. Liu, S. Sang, Q. Wu, Z. Lu, K. Liu, H. Liu, *Electrochim. Acta* 143 (2014) 340–346.
- [6] Y. Xiao, G. Zhan, Z. Fu, Z. Pan, C. Xiao, S. Wu, C. Chen, G. Hu, Z. Wei, *Electrochim. Acta* 141 (2014) 279–285.
- [7] L. Yan, Y. Xu, M. Zhou, G. Chen, S. Deng, S. Smirnov, H. Luo, G. Zou, *Electrochim. Acta* 169 (2015) 73–81.
- [8] L. Wu, S. Wu, Z. Xu, Y. Qiu, S. Li, H. Xu, *Biosens. Bioelectron.* 80 (2016) 59–66.
- [9] M. Xia, Q. Zhang, P. Pan, X. Zhong, H. Long, X. Tong, G. Liu, *Mater. Lett.* 160 (2015) 544–546.
- [10] Y. Zhu, Z. Chen, T. Gao, Q. Huang, F. Niu, L. Qin, P. Tang, Y. Huang, Z. Sha, Y. Wang, *Appl. Catal. B: Environ.* 163 (2015) 16–22.
- [11] M. Zeng, X. Zeng, X. Peng, Z. Zhu, J. Liao, K. Liu, G. Wang, S. Lin, *Appl. Surf. Sci.* 388 (2016) 352–358.
- [12] C. Lee, X. Wei, J.W. Kysar, J. Hone, *Science* 321 (2008) 385–388.
- [13] S.-W. Lee, C.-W. Lee, S.-B. Yoon, M.-S. Kim, J.H. Jeong, K.-W. Nam, K.C. Roh, K.-B. Kim, *J. Power Sources* 312 (2016) 207–215.
- [14] S.R. Shin, Y.C. Li, H.L. Jang, P. Khoshakhlagh, M. Akbari, A. Nasajpour, Y.S. Zhang, A. Tamayol, A. Khademhosseini, *Adv. Drug Deliv. Rev.* 105 (2016) 255–274.
- [15] Y. Yang, C. Han, B. Jiang, J. Iocozzia, C. He, D. Shi, T. Jiang, Z. Lin, *Mater. Sci. Eng. R: Rep.* 102 (2016) 1–72.
- [16] B. Zhang, Y. Wang, G. Zhai, *Mater. Sci. Eng. C: Mater. Biol. Appl.* 61 (2016) 953–964.
- [17] A.K. Geim, K.S. Novoselov, *Nat. Mater.* 6 (2007) 183–191.
- [18] X. Li, W. Cai, J. An, S. Kim, *Science* 324 (2009) 1312–1314.
- [19] J. Zhang, L. Huang, P. Liu, Y. Wang, X. Jiang, E. Zhang, H. Wang, Z. Kong, J. Xi, Z. Ji, *J. Alloys Compd.* 654 (2016) 71–78.
- [20] S.-Y. Ye, S.-W. Shen, L.-M. Ye, X.-L. Song, S.-C. Luo, *Mater. Sci. Semicond. Process.* 27 (2014) 397–403.
- [21] Y.-W. Zhang, H.-L. Ma, Q.-L. Zhang, J. Peng, J.-Q. Li, M.-L. Zhai, Z.-L. Yu, *J. Mater. Chem.* 22 (2012) 13064–13069.
- [22] J. Zhuang, W. Dai, Q. Tian, Z. Li, L. Xie, J. Wang, P. Liu, X. Shi, D. Wang, *Langmuir* 26 (2010) 9686–9694.
- [23] J.M. Macak, M. Zlamal, J. Krysa, P. Schmuki, *Small* 3 (2007) 300–304.
- [24] X.-W. Kang, S.-W. Chen, *J. Mater. Sci.* 45 (2010) 2696–2702.
- [25] A.E.R. Mohamed, S. Rohani, *Energy Environ. Sci.* 4 (2011) 1065–1073.
- [26] M. Faraji, N. Mohaghagh, *Surf. Coat. Technol.* 288 (2016) 144–150.
- [27] J. Paredes, S. Villar-Rodil, P. Solis-Fernandez, A. Martinez-Alonso, J. Tascon, *Langmuir* 25 (2009) 5957–5968.
- [28] P.-G. Ren, D.-X. Yan, X. Ji, T. Chen, Z.-M. Li, *Nanotechnology* 22 (2010) 55705–55712.
- [29] Z. Xie, X. Liu, W. Wang, X. Wang, C. Liu, Q. Xie, Z. Li, Z. Zhang, *Nano Energy* 11 (2015) 400–408.
- [30] P. Babeleon, A.S. Dequiedt, H. Mosefa-Sba, S. Bourgeois, P. Sibillot, M. Sacilotto, *Thin Solid Films* 322 (1998) 63–65.
- [31] Y. Lai, H. Zhuang, K. Xie, D. Gong, Y. Tang, L. Sun, C. Lin, Z. Chen, *New J. Chem.* 34 (2010) 1335–1340.
- [32] G. Allaiedini, E. Mahmoudi, P. Aminayi, S.M. Tasirin, A.W. Mohammad, *Synth. Met.* 220 (2016) 72–77.
- [33] G. Guo, Y. Hu, S. Jiang, C. Wei, J. Hazard. Mater. 223–224 (2012) 39–45.
- [34] M. Diak, M. Klein, T. Klimczuk, W. Lisowski, H. Remita, A. Zaleska-Medynska, E. Grabowska, *Appl. Catal. B: Environ.* 200 (2017) 56–71.
- [35] A. Vornvas, K. Pomoni, C. Trapalis, N. Todorova, *Mater. Sci.* 25 (2007) 809–816.
- [36] I.F. Ferguson, J.E. Kirwan, *Comput. Phys. Commun.* 5 (1973) 328–348.
- [37] L. Ainouche, L. Hamadou, A. Kadri, N. Benbrahim, D. Bradai, *Sol. Energy Mater. Sol. Cells* 151 (2016) 179–190.
- [38] Q. Xiang, J. Yu, P.K. Wong, *J. Colloid Interface Sci.* 357 (2011) 163–167.
- [39] F. Meng, Z. Sun, *Appl. Surf. Sci.* 255 (2009) 6715–6720.
- [40] B. Pant, P.S. Saud, M. Park, S.-J. Park, H.-Y. Kim, *J. Alloys Compd.* 671 (2016) 51–59.
- [41] H. Zhang, X. Lv, Y. Li, Y. Wang, J. Li, *ACS Nano* 4 (1) (2010) 380–386.
- [42] Y. Liu, L. Fang, H. Lu, Y. Li, C. Hu, H. Yu, *Appl. Catal. B: Environ.* 115–116 (2012) 245–252.
- [43] S. Huang, Z.-C. Si, X.-K. Lia, J.-S. Zou, Y.-W. Yao, D. Weng, *Sens. Actuators B* 234 (2016) 264–272.
- [44] G.-X. Hu, B. Tang, *Mater. Chem. Phys.* 138 (2013) 608–614.